LBL-35051
UC-404

Lawrence Berkeley Laboratory
UNIVERSITY OF CALIFORNIA

Materials Sciences Division

Presented at the Fourth International Conference on the Structure of Surfaces, Shanghai, China, August 16–19, 1993, and to be published in the Proceedings

Photoelectron Diffraction and Holography: Some New Directions

C.S. Fadley

August 1993

Prepared for the U.S. Department of Energy under Contract Number DE-AC03-76SF00098

DISCLAIMER

LBL-35051

PHOTOELECTRON DIFFRACTION AND HOLOGRAPHY: SOME NEW DIRECTIONS

Charles S. Fadley

Materials Sciences Division
Lawrence Berkeley Laboratory
University of California
Berkeley, California 94720
and
University of California at Davis
Department of Physics
Davis, California 95616

Acknowledgement

Work supported by the U.S. Department of Energy, Basic Energy Sciences, Materials Sciences Division under Contract DOE-AC03-76SF00098 and the Office of Naval Research under Contract N00014-90-J-1457 and N00014-92-J-1140.

Invited paper to appear in the Proceedings of
The Fourth International Conference on the Structure of Surfaces
Shanghai, August, 1993

PHOTOELECTRON DIFFRACTION AND HOLOGRAPHY: SOME NEW DIRECTIONS+

CHARLES S. FADLEY
Department of Physics, University of California-Davis, Davis, CA 95616
Materials Sciences Division, Lawrence Berkeley Laboratory, Berkeley, CA 94720

ABSTRACT

Photoelectron diffraction has by now become a versatile and powerful technique for studying surface structures, with special capabilities for resolving chemical and magnetic states of atoms and deriving direct structural information from both forward scattering along bond directions and back-scattering path length differences. Further fitting experiment to theory can lead to structural accuracies in the $\pm$0.03 Å range. Holographic inversions of such diffraction data also show considerable promise for deriving local three-dimensional structures around a given emitter with accuracies of $\pm$0.2-0.3 Å. Resolving the photoelectron spin in some way and using circularly polarized radiation for excitation provide added dimensions for the study of magnetic systems and chiral experimental geometries. Synchrotron radiation with the highest brightness and energy resolution, as well as variable polarization, is crucial to the full exploitation of these techniques.

INTRODUCTION

Photoelectrons emitted from core levels represent localized sources of outgoing waves which can then scatter from nearby atoms to produce diffraction patterns. We will here consider several new directions for using such diffraction patterns to determine surface atomic positions, as well as surface magnetic structures [1-5]. The analysis of such data in a more recently suggested holographic manner so as to directly image atoms in three dimensions [6,7] will also be considered. The special benefits that synchrotron radiation brings to such studies will also be pointed out.

PHOTOELECTRON DIFFRACTION--BASIC CONCEPTS

Photoelectron diffraction patterns are by now well known and much studied, and have lead to the increasing use of this technique for surface structure studies [1-5]. The fundamental measurement is illustrated in Fig. 1. A photoelectron is emitted from a core level, and its intensity is measured as a function of its direction or its energy above a single-crystal sample, yielding what can be termed scanned-angle or scanned-energy data, respectively. In terms of the electron wave vector $\underline{k}$, this is equivalent to measuring intensity as a function of its direction $\hat{k} = \underline{k}/|\underline{k}|$ or its magnitude $k = |\underline{k}|$. Intensity variations are produced by the interference of the unscattered or direct wave component ϕ_o and the various scattered-wave components ϕ_j.

The resulting photoelectron intensity as a function of wave vector can be written in a simple single scattering picture as [1b,1c]:

$$I(\underline{k}) \propto |\phi_o + \Sigma_j \phi_j|^2$$

$$\propto |\phi_o|^2 + \Sigma_j(\phi_o^* \phi_j + \phi_o \phi_j^*) + \Sigma_j \Sigma_k \phi_j \phi_k^* \ , \qquad (1)$$

where ϕ_j and ϕ_k are arbitrary scattered waves. For the illustrative case of photoelectron emission from an s subshell into an outgoing ϕ_o with p character, the individual wave components here can be written out more explicitly in terms of (cf. Fig. 1): dipole matrix elements that are for linearly polarized radiation proportional to the dot product of the polarization direction ($\hat{\epsilon}$) and the relevant emission direction ($\hat{k}$ or $\underline{r}_j/r_j = \hat{r}_j$); inelastic exponential decay factors $\exp(-L/2\Lambda_e)$, with L equal to the total length for some path below the surface and Λ_e equal to the inelastic attenuation length for photoelectron intensity; scattering factors $f_j(\theta_j,r_j)$ involving both an amplitude $|f_j(\theta_j,r_j)|$ and a phase shift $\Psi_j(\theta_j,r_j)$ that are functions of the scattering angle θ_j, and, in more accurate spherical-wave scattering, also of the distance r_j to a given scatterer; Debye-Waller factors W_j that allow for attenuation of interference due to vibrational effects; and finally, phase shifts due to path length differences of the form $\exp[ikr_j]\exp[-i\underline{k}\cdot\underline{r}_j] = \exp[ikr_j(1-\cos\theta_j)]$. All structural information is thus contained in this last exponential factor, with the path length difference between ϕ_o and ϕ_j being given by $r_j(1-\cos\theta_j)$. Eq. 1 thus can be rewritten as:

$$I(\underline{k}) \propto |(\hat{\epsilon}\cdot\hat{k})\exp(-L_o/2\Lambda_e) + \Sigma_j(\hat{\epsilon}\cdot\hat{r}_j/r_j)|f_j(\theta_j,r_j)|W_j\exp(-L_j/2\Lambda_e)$$

$$\cdot\exp[i\{kr_j(1-\cos\theta_j)+\Psi_j(\theta_j,r_j)\}]|^2 \ , \qquad (2)$$

or, in more convenient notation:

$$I(\underline{k}) \propto |F_o + \Sigma_j F_j \exp[-i\underline{k}\cdot\underline{r}_j]|^2 \ , \qquad (3a)$$

with

$$F_o(\underline{k}) = (\hat{\epsilon}\cdot\hat{k})\exp(-L_o/2\Lambda_e) \qquad (3b)$$

$$F_j(\underline{k},\underline{r}_j) =$$

$$(\hat{\epsilon}\cdot\hat{r}_j/r_j)|f_j(\theta_j,r_j)|W_j\exp(-L_j/2\Lambda_e)\exp[ikr_j]\exp[i\Psi_j(\theta_j,r_j)] \ . \qquad (3c)$$

Here, one portion of the phase factor due to path length ($\exp[ikr_j]$) is now incorporated into the F_j's. Eqs. 3 can also be formally generalized to include multiple scattering [7a,8d], in which case each F_j must include a sum over the various single and multiple scattering pathways m with different total lengths L_{mj} that terminate in scatterer j just before going to the detector; within each multiple-scattering pathway, there also will be products of successive path-length phase factors and scattering factors. For emission from a subshell other than s (i.e. for $l_{initial} > 0$), the above expressions become more complex due to sums

over initial and final magnetic quantum numbers and interference between the two final-state channels $l_{final} = l+1$ and $l-1$ that are allowed by the dipole selection rules [8a,8d,9].

Expanding the square in Eq. 3a now yields

$$I(\underline{k}) \propto |F_o|^2 + \Sigma_j [F_o^* F_j \exp\{-i\underline{k}\cdot\underline{r}_j\} + F_o F_j^* \exp\{i\underline{k}\cdot\underline{r}_j\}]$$

$$+ \Sigma_j \Sigma_k [F_j^* F_k \exp\{i\underline{k}\cdot(\underline{r}_j-\underline{r}_k)\} + F_j F_k^* \exp\{-i\underline{k}\cdot(\underline{r}_j-\underline{r}_k)\}] \quad . \qquad (4)$$

$|F_o|^2$ is thus simply proportional to $I_o(\underline{k})$: the intensity in the absence of any scattering. A normalized intensity function $\chi(\underline{k})$ can now be calculated, very much as in the analysis of extended x-ray absorption fine structure (EXAFS), with one choice being [7a]:

$$\chi(\underline{k}) = [I(\underline{k}) - I_o(\underline{k})]/I_o(\underline{k})^{1/2} \quad , \qquad (5)$$

and this yields

$$\chi(\underline{k}) \propto (|F_o|)^{-1} \Sigma_j [F_o(\underline{k})^* F_j(\underline{k}) \exp\{-i\underline{k}\cdot\underline{r}_j\} + F_o(\underline{k}) F_j(\underline{k})^* \exp\{i\underline{k}\cdot\underline{r}_j\}]$$

$$+(|F_o|)^{-1} \Sigma_j \Sigma_k [F_j(\underline{k})^* F_k(\underline{k}) \exp\{i\underline{k}\cdot(\underline{r}_j-\underline{r}_k)\} + F_j(\underline{k}) F_k(\underline{k})^* \exp\{-i\underline{k}\cdot(\underline{r}_j-\underline{r}_k)\}], \qquad (6)$$

where the r_j or r_k dependence of F_j or F_k, respectively, in spherical-wave scattering have not been indicated explicitly. This form is useful in considering holographic analyses of diffraction.

Another common approximation is to assume that the scattered waves ϕ_j and ϕ_k are small in amplitude with respect to ϕ_o, so that the cross terms $\phi_o^* \phi_j$ and $\phi_o \phi_j^*$ in Eq. 1 dominate the structural information. This directly leads via Eqs. 3 and 6 to

$$\chi(\underline{k}) \propto 2\Sigma_j (\hat{\epsilon}\cdot\hat{r}_j/r_j) |f_j(\theta_j)| W_j \exp(-L_j/2\Lambda_e)$$

$$\cdot \cos[kr_j(1-\cos\theta_j) + \Psi_j(\theta_j, r_j)] \quad . \qquad (7)$$

This form directly shows that Fourier transforms of scanned-energy data along some direction $\hat{k}$ and over some interval Δk

$$F_{\Delta k}(\hat{k}, r) \propto \int_{\Delta k} \chi(\underline{k}) \exp[-ikr] dk \quad , \qquad (8)$$

should be useful for deriving path length differences $r = r_j(1-\cos\theta_j)$, a result that has been discussed and used in a number of previous studies [4,10].

There are several important characteristics of such photoelectron diffraction patterns, as summarized below. More detailed discussions with illustrative examples appear elsewhere [1-5].

-<u>Measurement of intensities</u>: In general, core peak intensities must be

measured by accumulating data for the full spectrum and then accurately allowing for the inelastically-scattered background on which the elastic intensity rides. At a minimum, one must accumulate three energy points above, on, and below the peak to make this background correction. Inasmuch as the background is known to exhibit diffraction features that can be much different from those of the elastic intensity [11], ignoring this correction as suggested recently [12] could introduce significant errors in the diffraction pattern and is not expected to be a generally reliable method.

-Atom specificity: The measurements are inherently atom-specific, since core level energies can always be found that are unique to a given atom. Thus, the local structure around each of the atomic types in a sample can be studied.

-Chemical-state specificity: For many systems, core levels furthermore exhibit chemical shifts or surface shifts, so that the structure around different chemical/surface states of the same atom can in principle be studied separately. This has been applied for example to distinguishing surface and bulk metal atoms [13a], the different sites in adsorbed molecules [13b] or atoms [13c], and different layers near epitaxial interfaces and surfaces [13d]. This application often requires energy resolutions in the 0.1-0.3 eV range, and is thus well-suited to synchrotron radiation studies.

-Spin specificity: In atoms or molecules with a net magnetic moment, exchange-produced splittings of core levels in which the spin-up and spin-down photoelectrons are separated in energy can also arise [14]. The degree of spin polarization in such multiplet peaks is defined by $P = [I(\uparrow)-I(\downarrow)]/[I(\uparrow)+I(\downarrow)]$, with $I(\uparrow)$ and $I(\downarrow)$ equal to the spin-up and spin-down intensities, respectively. Multiplet polarizations are internally-referenced to the orientation of the emitting magnetic moment. If on the other hand circularly polarized radiation is used to excite spin-orbit-split core levels, a significant degree of spin polarization (now externally-referenced to the direction of incidence of the light) can be induced in the outgoing photoelectrons [15]. Such measurements require synchrotron radiation, as discussed further below. Finally, an externally-referenced spin detector can be used to directly measure the spin polarization over a given core spectrum [16]. These ways of inducing or measuring spin selectivity suggest the use of spin polarized photoelectron diffraction in the study of magnetic materials, as amplified below. In order to enhance magnetic scattering effects, kinetic energies of approximately 100 eV are required [14], thus again in general implying synchrotron radiation for excitation.

-Well-defined and controllable emission process: Although similar short-range-order diffraction is found in Auger electron emission [1,2], the electron excitation of Auger processes [17], quasi-elastic back-scattered Kikuchi electrons [1c,2a,18], and diffuse LEED and fractional-order LEED [19], the physics of the emission process is best understood for photoelectron emission. That is, the initial core level is described by a given l value, and the dipole excitation leads to only

two interfering channels of $l \pm 1$. Thus, theoretical modeling can be the most accurate for photoelectron diffraction and holography. Varying both the polarization and energy of the exciting photon also can be used to emphasize different scatterers or aspects of the emission or scattering process.

-Simple forward scattering: In measurements at photoelectron kinetic energies of about 500 eV or higher, the scattering amplitude $|f_j(\theta_j,r_j)|$ is highly peaked in the forward direction (i.e. near $\theta_j = 0$). Many studies have by now shown that such forward scattering or forward focussing peaks can be directly used to determine bond directions for adsorbed molecules [1,3] and low-index directions for single crystals and epitaxial overlayers [1,2]. As an illustration of the sensitivity of such high-energy patterns to different surface structures, Fig. 2 shows the full 2π intensity distributions above three different surfaces, in stereographic projection: fcc Ni(001) [20], hcp Ru(0001) [21], and the textured surface of highly oriented pyrolytic graphite with a preferred (0001) orientation [22]. Such forward scattering peaks have also been found to be sensitive to surface pre-melting phenomena [23]. The higher kinetic energies required for this kind of measurement have led to its being performed primarily with laboratory x-ray sources in the 1.2-1.5 keV range, but higher brightness synchrotron radiation sources in the 500-1500 eV range would be equally useful for this work.

-Back scattering: In measurements at lower photoelectron kinetic energies of less than about 300 eV, there is also a significant degree of back scattering, and this can be used in several ways to extract structural information concerning atoms that are "behind" the emitter as viewed by the detector [1,4,5,10,24]. Synchrotron radiation is again necessary to insure sufficiently low kinetic energies in such studies.

- Single scattering and multiple scattering analysis: In a number of prior studies, it has been found that a simple single scattering model such as that outlined above is able to predict most of the structure in diffraction patterns, and thus it also can be useful for deriving some structural information. However, multiple scattering effects can be strong in both forward scattering along high-density rows of atoms (where events of order up to the number of scatterers between emitter and scatterer may have to be considered [8d]) and back scattering at lower energies (where events up to third order are found to be essential for predicting all diffraction features [8d,e]). This is illustrated in Fig. 3, where experimental and calculated full diffraction patterns above a Ni(001) surface are shown [20]. The experimental pattern away from low-index directions is reasonably well predicted by single scattering theory, but both the intensity and width of the low-index forward scattering peaks are much overestimated in this simple model. Multiple scattering theory by contrast predicts all aspects of the diffraction pattern very well, even though only five emitter layers were included in this simulation.

-Path-length differences: Another direct form of structural information that can be obtained by virtue of the strong single scattering character

of photoelectron diffraction is the path length difference associated with a given scatterer j: $r_j(1-\cos\theta_j)$ [1,4,5,10,24]. As noted in connection with Eq. 8, this requires Fourier transforming scanned-energy data over some interval Δk, and in turn implies the use of synchrotron radiation so as to be able to vary energy (and thus k) in small steps. The presence of the scattering phase shift $\Psi_j(\theta_j,r_j)$ in Eq. 7 also can lead to errors in path length differences derived in this way, unless a correction is somehow made for it in doing the transform [10]. However, Zheng and Shirley [4c] have recently found highly accurate path length differences with Eq. 8 for properly chosen adsorbate experimental geometries.

Two interesting variations in the use of Eq. 8 have recently been proposed as methods of making first estimates of nearest-neighbor positions relative to an adsorbate [24]. In the first due to Fritzsche and Woodruff [24a], $\chi(\underline{k})$ data is intentionally taken with poor angular and energy resolution so as to reduce the importance of scatterers further from the emitter and/or away from the back-scattering direction. Eq. 8 is then applied to such data, with the result that a back-scattering nearest-neighbor peak will be strongest in the Fourier transform when the detection direction $\hat{k}$ is parallel to the emitter-to-nearest neighbor direction. Scanning over several $\hat{k}$ values thus appears capable of locating this back-scattering direction to within a few degrees [24a], in a manner very similar to forward scattering at higher energies. The second method due to Hofmann and Schindler [24b] uses the same philosophy but attempts to correct in a single scattering model for anisotropies in the outgoing unscattered wave and the scattered wave, as well as for the scattering phase shift. This is done by replacing the phase factor exp[-ikr] in Eq. 8 by a theoretical chi function $\chi^{(1)}_{theo}(\underline{k},\underline{r})$ calculated with a single substrate scatterer at various positions $\underline{r}$ with respect to the adsorbate emitter:

$$F'_{\Delta k}(\hat{k},\underline{r}) \propto \int_{\Delta k} \chi_{expt}(\underline{k})\chi^{(1)}_{theo}(\underline{k},\underline{r})dk \quad . \tag{8a}$$

From the simplest form for χ_{theo} given in Eq. 7, it is clear that this integral should attempt to project out from χ_{expt} that component of it due to a given scatterer, and that corrections for the form of the outgoing and scattered waves are implicitly included. (This procedure is very similar in philosophy to the scattered-wave included Fourier transform (SWIFT) method proposed previously for holographic image formation from scanned-angle data by Tonner, Saldin, and co-workers [25], as will be discussed further below. The SWIFT method divides χ_{expt} by quantities in $\chi^{(1)}_{theo}$ to correct for outgoing and scattered waves from a given type of scatterer, leaving a pure sinusoidal phase factor $\exp[i\underline{k}\cdot\underline{r}]$ in the integral.) The six-dimensional function F' in Eq. 8a is found to tend to peak when $\underline{r}$ is near the scatterer position. However, in order to adequately estimate this position, it has been found necessary to sum the results of transforms along approximately ten directions $\hat{k}_q$ according to the empirically useful formula [24b]

$$C(\underline{r}) = \Sigma_q \exp[F'_{\Delta k}(\hat{k}_q,\underline{r})r] \quad . \tag{8b}$$

Here, the exponential in r is used to deemphasize divergences in F'

occurring near the origin. A total number of data points of about 1000 is thus needed for such a structure estimate. A more rigorously derivable method for summing such Fourier transforms of scanned-energy data so as to derive atomic positions in three dimensions will be discussed under photoelectron holography below.

-Accurate surface structures: In a growing number of studies to date, it has been possible also to determine more detailed surface structures by fitting experimental diffraction patterns of either the scanned-angle or scanned-energy type to theoretical simulations for various possible trial geometries [1,2a,4,5,8b,24]. Direct structural information from forward scattering or back-scattering path length differences can often be used to eliminate various possible structures and arrive at a very good guess for the final trial-and-error search. Theoretical calculations have been carried out at both the single scattering [1,2a] and more accurate multiple scattering [1,4,5,8] levels. With careful analysis of such fits, e.g., via R factors, accuracies in the approximately $\pm$0.03Å range have been obtained. However, further work is needed to speed up such structure searches and the multiple scattering calculations needed for the highest ultimate accuracy. Finally, more rapid data acquisition methods are also called for; these will benefit from next-generation higher-brightness synchrotron sources as well.

PHOTOELECTRON HOLOGRAPHY

More recently, it has been suggested by Szöke [6] that such photoelectron diffraction patterns can be treated as holograms, with the unscattered wave ϕ_o being identified as the reference wave of the hologram, and the scattered waves ϕ_j being identified as the object waves. A diffraction pattern that is somehow measured over a relatively large number of points in $\underline{k}$ space which may involve varying both direction and energy is then converted into a direct three-dimensional image of the atoms surrounding a given atom using a Fourier-transform-like integral. The hologram is in this interpretation just the intensity $I(\underline{k})$, or more conveniently the normalized function $\chi(\underline{k})$. The holographic analysis of diffraction data is in a much more developmental stage, but several encouraging experimental studies have been carried out to date [12,26-31].

The first holographic imaging procedure to be demonstrated quantitatively is due to Barton [7a]. It makes use of scanned-angle data at a single energy, for which the Helmholtz-Kirchoff theorem from optics is used to calculate the atomic image $U(\underline{r})$ (actually the source wavefield) from:

$$U(x,y,z) \propto \left| \iint_S \chi(\underline{k}) \exp[i\underline{k}\cdot\underline{r}] d\sigma_k \right| , \qquad (9)$$

where the integral on the direction of $\underline{k}$ is over the spherical surface on which the hologram is measured. Note that $\chi(\underline{k})$ has here been multiplied by the complex conjugate of the direction-dependent part of the phase factor due to path length difference $\exp[-i\underline{k}\cdot\underline{r}]$, and that the

magnitude of $\underline{k}$ is fixed. Applying Eq. 9 to $\chi(\underline{k})$ as written in Eq. 6 them immediately predicts the existence of both real and twin images at $\pm\underline{r}_j$, as well as weaker self-interference images at $\pm(\underline{r}_j-\underline{r}_k)$, both potentially complicating features in structural studies. Self-interference effects have been predicted by Thevuthasan et al. [32] to be generally only $\leq$10-20% as strong as the real+twin images, although they may not always be negligible. Further taking the z axis to be along the symmetry axis of the hologram and thus usually also to be perpendicular to the surface and then projecting $\chi(\underline{k})$ onto the k_x,k_y surface plane permits doing a two-dimensional Fourier transform with z as a variable parameter to yield the image U in a given z plane as [7a]:

$$U(x,y,z) \propto \left|\iint\{\chi(\underline{k})\exp[ik_z z]\}\exp[i(k_x x + k_y y)]dk_x dk_y\right| . \qquad (10)$$

If the full opening angle of the hologram as centered on the z-axis normal to the surface is defined to be α, it can further be shown [7a,7b] that the uncertainties with which positions can be determined in the three coordinates are given by: $\Delta x = \Delta y = 1.22\pi/[k\sin(\alpha/2)] = 0.61\lambda_e/\sin(\alpha/2)$ in the surface plane and $\Delta z \simeq 4\pi/[k\sin^2(\alpha/2)] = 2\lambda_e/\sin^2(\alpha/2)$ perpendicular to the surface plane, where λ_e is the electron de Broglie wavelength. These uncertainties can also be inversely related via the Uncertainty Principle to the ranges Δk_x, Δk_y, and Δk_z that are spanned by the hologram [26b,33]: $\Delta x \simeq 1/\Delta k_x$, $\Delta y \simeq 1/\Delta k_y$, and $\Delta z \simeq 1/\Delta k_z$. It has also been argued that the effective Δk for a given coordinate of a certain scatterer may be smaller at higher energies because the holographic fringes are strong only near the forward scattering direction [26b].

Holographic images also may be distorted due to anisotropy in the amplitudes of both the reference wave ϕ_o and the scattered waves ϕ_j, as well as the often significant phase shifts Ψ_j due to scattering. Possible solutions to these problems are to eliminate or correct regions of the hologram that are most non-ideal, as for example, over the forward scattering peaks [26,32a]. As one example of this, Fig. 4 shows experimental and theoretical images for the well-defined test case of c(2x2)S on Ni(001) obtained by Thevuthasan et al. [27] in two different symmetry planes, as shown in the atomic geometry. Here, data for S 2p emission at 1327 eV have been obtained for takeoff angles between 10° and 50° above the surface in order to avoid strong forward scattering and multiple scattering effects that may occur for emission directions more nearly parallel to the surface. The images of the nearest-neighbor sulfur atoms are clear in both experiment and theory, and there is good agreement as to the degree of shift relative to the true positions of about 1.0 Å. Similar images have been found with a corresponding analysis of Na 1s emission at a lower energy of 182 eV from c(2x2)Na on Al(001) by Osterwalder and co-workers [31].

To improve the image positions, it is necessary to somehow correct for anisotropic scattering amplitudes and/or phase shifts in doing the image-producing transform [34]. One correction method proposed by Tonner, Saldin and co-workers [34a] is simply to normalize $\chi(\underline{k})$ by a

generalized scattered-wave strength F_j during the integration, which yields a new image function U':

$$U'(x,y,z) \propto \left| \iint \{\chi(\underline{k}) \exp[ik_z z]/F_j(\underline{k},\underline{r})\} \exp[i(k_x x + k_y y)] dk_x dk_y \right| \quad . \quad (11)$$

This has been termed the scattered-wave-included Fourier transform (SWIFT) method. In practice, this procedure has to date generally involved simply dividing by a plane-wave or spherical-wave scattering factor, which may then have to be adjusted with position in space so as to allow for the different types of scatterers present [27a-c,34]. The latter adjustment thus requires some advance knowledge of the structure, or an iterative approach. F_j also can in principle allow for the anisotropy in the outgoing reference wave, as is implicit in the factor $\hat{\epsilon} \cdot \hat{r}_j$ in Eq. 3c; this more general type of correction has been applied for the first time to experimental data from $CoSi_2$(111) by Zhou et al. [28].

The overlap of real and twin images is a problem shared with optical holography, but it is potentially more serious in images of surface structures, since the surface inherently breaks the inversion symmetry along its normal, and thus the twins of substrate atoms may overlap the regions in space occupied by adsorbate or overlayer atoms. One solution to this problem is to note that, for some cases, the region of the hologram most strongly affected by some atom at $\underline{r}$ is well localized in a solid-angle region centered on $\underline{r}$; this was first demonstrated in theoretical simulations by Saldin et al. [35]. Analyzing only this portion of the hologram then may lead to an image in which the twin from another atom at $-\underline{r}$ is suppressed, as suggested by Saiki et al. for scanned-angle data from cases dominated by forward scattering [36]. For back-scattering cases at lower energies, Tong et al. [34b] have also proposed analyzing scanned-energy data over only small windows in direction in order to emphasize a single scatterer behind the emitter.

In Fig. 5, we show the effects of simultaneously using these last two image improvement procedures, again for the case of c(2x2)S/Ni(001) [27c]. Only the right half of the hologram has been analyzed to focus on the position of the nearest neighbor along +x, and the SWIFT procedure has been applied in doing the image formation. The agreement between experiment and theory is again excellent, and the peak positions have improved to within about 0.3 Å of the known structure. This example thus suggests that even single-energy holographic images for adsorbate overlayers or thin epitaxial layers can be obtained with sufficient accuracy to be used for ruling out many possible structures and providing excellent starting points for more accurate final trial-and-error refinements. Other single-energy, SWIFT-corrected results for bulk $CoSi_2$ at 700 eV are also encouraging [28]. However, previous studies on multilayer bulk specimens of Cu [26a], Si [27a], and Ni [20] at higher single energies suggest that the presence of inequivalent emitters in several layers can lead to strong image distortions along forward scattering directions.

A more general approach for suppressing twins, as well as other deleterious effects in images, has also been suggested by Barton [7c], and it involves making phased summations of transforms of scanned-angle data obtained at different energies E_i with wave vectors k_i according to:

$$U''(x,y,z) \propto \left|\Sigma_i \exp[-ik_i r] \iint_S \chi(\underline{k}_i)\exp[i\underline{k}_i \cdot \underline{r}]d\sigma_k\right| \quad (12a)$$

$$\propto \left|\Sigma_i \exp[-ik_i r] \iint \{\chi(\underline{k}_i)\exp[ik_{iz}z]/F_j(\underline{k}_i,\underline{r})\}\right.$$

$$\left.\cdot\exp[i(k_{ix}x + k_{iy}y)]dk_x dk_y\right| \ . \quad (12b)$$

This sum can in principle be performed either with or without correction for the outgoing and scattered waves, although it has been included above in dividing again by $F_j(\underline{k},\underline{r})$ in Eq. 12b. In doing this sum, we have multiplied by the conjugate of the remaining phase factor due to path length difference exp[ikr], with $\chi(\underline{k})$ containing such factors inside of the F_j's (cf. Eqs. 2 and 3). The sum on k_i now varies the magnitude of $\underline{k}$, and selects out peaks at r_j in space for which $\chi(\underline{k})$, through the F_j's, contains phase factors $\exp[ikr_j]$. This method has been demonstrated to suppress twin images [7c,27b], most multiple scattering effects [7c], and self-interference effects [32b]. For example, encouraging experimental images have been obtained for bulk Cu(001) by Terminello et al. [29a] and bulk Pt(111) by Petersen et al. [29b].

As an illustration of how well images can be improved by this summed-energy approach, we show in Fig. 6 a theoretical simulation of images for the same c(2x2)S/Ni(001) system [32b]. The sum was over 13 energies between 862 and 1324 eV, with a constant δk step of 0.3 $Å^{-1}$. The hologram was here calculated over the region from 30° above the surface to normal, which should be the most nearly ideal portion of it, with weak, more isotropic, single scattering being dominant. Even with no scattered-wave corrections, the peak positions are here in excellent agreement with the known structure, the next-nearest-neighbor S atoms are somewhat visible, and the five Ni atoms underneath a typical S emitter are clearly seen. This simulation makes the use of such summed-energy analyses look extremely encouraging for adsorbate and thin overlayer structure studies, although the Ni atoms below the S emitter will probably be more weakly imaged in experiment due to the fact that no vibrational effects were included in these calculations.

An important question that immediately arises is how many energies need to be summed over, and how small the steps δk between them need to be to optimally reduce image aberrations and artifacts. Thevuthasan et al. have found in various theoretical simulations that about 10 energies spaced by a constant δk are sufficient to yield essentially complete twin and multiple scattering suppression [27b,32b]. In addition, the size of δk must be small enough to push artifacts (related to aliasing in standard Fourier transform theory) outside of the range of

interatomic distances that are to be studied. The behavior of these artifacts is illustrated in Fig. 7, where images in the xy plane of c(2x2)S/Ni(001) are shown for different numbers of energies spanning the range from 862 to 1324 eV. Only the right half of the hologram has been analyzed (as in Fig. 5) to emphasize the real image due to the nearest-neighbor along +x. In going from 1 to 3 to 5 to 7 to 13 energies, we see a gradual suppression of twin-related features in the left half of the image, as expected. But anomalous features remain in circles at multiples of $\pi/\delta k$ away from the origin and these are fully moved out of the region of interest only in the last panel with 13 energies. Thus, such criteria on the choice of δk are crucial if image artifacts are to be suppressed.

Tong and co-workers [37] have also proposed a similar holographic approach for analyzing scanned-energy data so as to simultaneously correct for scattered-wave anisotropies and eliminate twin and multiple-scattering effects. This method makes use of a number of scanned-energy diffraction curves that are then Fourier transformed, summed, and used to determine the real-image positions of certain atoms. What is being done in this procedure is to Fourier transform a $\chi(\underline{k}_q)$ obtained along the direction $\hat{k}_q$ over small steps in k_q first and then to carry out a phased sum over several larger steps in direction, as shown below:

$$U''''(x,y,z) \propto \left|\Sigma_q \exp[i\underline{k}_q\cdot\underline{r}]\int_{\Delta k_q}\chi(\underline{k}_q)\exp[-ik_q r]dk_q\right| . \qquad (13)$$

Corrections for scattering amplitudes and/or phase shifts can also be included in this integral, in the same spirit as indicated in Eq. 12. Encouraging atomic images have been obtained using this approach for ($\sqrt{3}$ x $\sqrt{3}$)Al on Si(111) by Wu et al. [30]. This equation is similar to Eq. 8b, except that the sum on directions now has a phase that is more clearly related to a three-dimensional holographic transform.

Comparison of Eqs. 12a and 13 makes it clear that the approaches of Barton and Tong are fundamentally equivalent, in that they just interchange the order of integration and summation, with the same overall phase factor of $\exp[-ikr]\exp[i\underline{k}\cdot\underline{r}]_{\hat{}} = \exp[-ikr(1-\cos\theta)]$. However, the first emphasizes finer steps in $\hat{k}$ and the other finer steps in k. Thus, if both are carried out over equivalent ranges of Δk_x, Δk_y, and Δk_z, one would expect corresponding resolutions in the coordinates x, y, and z, provided that the $\underline{k}$ steps are sufficiently small in all directions to avoid spurious features due to the non-cancellation of twin and multiple scattering features (cf. Fig. 7). If applied correctly, both methods should be equally capable of suppressing twin and multiple scattering effects. For a given image accuracy and scope in $\underline{r}$ space, it is also expected that these two approaches would require about the same size of data set: something like 3,000-5,000 intensities with allowance for surface symmetry.

In fact, these two methods of summing/integrating over intensities are really just the two limits of a continuous range of choices in sampling a given volume of $\underline{k}$ space, as illustrated in Fig. 8 [38]. Here are shown the holographic images for a simple pyramidal cluster of Cu

atoms as computed according to Eq. 12 (or equivalently Eq. 13), with no scattered-wave corrections. The sampling of $\underline{k}$ space has been varied so as to change from fine steps in direction and course steps in energy ("scanned-angle" data) to course steps in direction and fine steps in energy ("scanned-energy" data). However, the total number of data points has been kept constant at about 4,000-4,500 over the symmetry-reduced 1/8 of the hemisphere that would be necessary to study for this problem. It is clear that similar images can be obtained over a range of choices between scanned-angle and scanned-energy, but that going to too widely spaced choices in direction (panel (d)) or energy (see Fig. 7) can cause image deterioration. Thus, a range of data taking options should be available in photoelectron holography.

Some advantages of the scanned-angle/summed-energy approach should be pointed out however: Scanning a monochromator (and perhaps also an undulator gap in next-generation experiments) is more difficult than scanning a specimen goniometer [1] or using a display analyzer [29] to accumulate data over a broad range of solid angle at one time. Also, Auger electrons at fixed kinetic energy often interfere with measuring photoelectron intensities continuously over a sufficient range of energies, but this problem might be avoided by choosing suitable energy increments in a scanned-angle approach. In either the scanned-angle or scanned-energy approach, intensities have to be normalized for variations in photon flux with time and photoelectric cross sections with energy, as well as for any other purely instrumental effects on $\chi(\underline{k})$, but this procedure is probably somewhat simpler in the scanned-angle mode.

Finally, we comment on the extra amount of data required in photoelectron holography relative to more standard applications of photoelectron diffraction. It has been suggested that this additional effort is unnecessary, as methods such as that embodied in Eqs. 8a,b can already be used to derive reasonably good first estimates of nearest-neighbor positions for subsequent trial-and-error structure determinations [24]. However, these simpler approaches do not have the potential of getting information on neighbors further away, whereas holography does [cf. Figs. 6-8 and refs. 28-30]. Also, some of these approaches [24] seem limited to emission from well-defined adsorbate overlayers, but not to be suitable for buried species, e.g. in epitaxial overlayers. Finally, the net increase in data required appears to be only about 3-5x, a factor which should be tractable with higher-brightness synchrotron radiation sources.

PHOTOELECTRON DIFFRACTION WITH CIRCULARLY-POLARIZED RADIATION

If instead of linearly-polarized radiation, left or right circularly-polarized radiation is used for core-level excitation, two distinct kinds of circular dichroism (CD) can occur: one due to emission in some sort of chiral experimental geometry (what we will call "normal" dichroism), and one due to spin-orbit splitting in the presence of an external magnetic field (magnetic CD or MCD) [15]. The latter is based on the well-known Fano effect first discussed for atoms: left and right

polarized radiation can cause preferential excitation of spin-up or spin-down electrons, even if there were equal populations of the two types in the initial spin-orbit-split core states. In either case, the degree of dichroic asymmetry can be measured as a function of $\underline{k}$ via

$$A^{CD}(\underline{k}) = [I^{RCP}(\underline{k}) - I^{LCP}(\underline{k})]/[I^{RCP}(\underline{k}) + I^{LCP}(\underline{k})] \quad , \qquad (14)$$

where I^{RCP} and I^{LCP} are the intensities measured with right and left polarized light, respectively. Very few measurements of the $\underline{k}$ dependence of A^{CD} in core-level emission have been made to date, but we illustrate the types of effects expected with two examples.

Bansmann and co-workers [39a] have studied normal CD in C 1s emission from CO adsorbed on Pd(111) in a chiral experimental geometry. Some of their experimental data as a function of electron emission angle θ are shown in Fig. 9, together with theoretical calculations based on several models. The effects are quite pronounced, being as large as $\pm$75% variations in A^{CD}. The three theoretical curves all agree reasonably well with the data: two are based upon treating an isolated CO molecule only, and one includes the effect of the Pd substrate. Two of these curves (------ and - --- -) have been calculated by Westphal et al. [39b] in a multiple-scattering diffraction picture of the outgoing wave, thus emphasizing the fact that <u>it is only through photoelectron scattering and diffraction from neighboring atoms that normal circular dichroism can manifest itself in core-level emission</u>. Diffraction theory including the effects of the underlying Pd atoms (- --- -) shows that the substrate could produce noticeable effects on such data, especially at lower energies for which back scattering is more important, but there are as yet no conclusive experimental data indicating such effects. The future measurement of circular dichroism in core emission with synchrotron radiation from insertion devices designed to produce high-brightness circularly-polarized radiation, coupled with analysis in terms of more accurate cluster-based multiple-scattering calculations [8b-d], thus represents a very interesting new direction of study in photoelectron diffraction.

MCD in core-level emission has so far been studied only for a few cases, and then only with a fixed emission direction. In Fig. 10, we show the first data of this type due to Baumgarten et al. [40a] for Fe $2p_{1/2,3,2}$ emission from Fe(110). In the lower part of (a) are shown two partial spectra obtained with the sample magnetization parallel to- and anti parallel to- the direction of helicity of circularly-polarized radiation; this is equivalent to changing from right to left polarization in the frame of the sample. The full spectrum in (a) represents an average over the two magnetizations. In (b), A^{CD} is plotted, and it is clear that significant effects of the order of a few percent are seen, even if they are much smaller than those found for normal CD in Fig. 9 Similar results have been obtained by Waddill et al. [40b] for Fe 2p emission from thin overlayers of Fe on Cu(001), again for a fixed direction of emission. Both sets of data have been qualitatively explained in terms of preferential excitation of photoelectrons of one spin or another in the $2p_{1/2}$ and $2p_{3/2}$ peaks,

combined with a spin-dependent splitting in the core level that is probably linked to multiplet effects. However, the analysis of such MCD data has not yet included interference between the l_{final} = 0 and 2 photoelectron channels, nor has any spin-dependent final-state scattering and diffraction been considered. It is also clear that normal CD can co-exist with MCD, and that both types of effect in general need to be considered simultaneously [39]. Thus, future studies in which both normal CD and MCD are measured over a range of $\underline{k}$ and analyzed more precisely with inclusion of both of these effects represent an important area of future development in photoelectron diffraction.

PHOTOELECTRON DIFFRACTION/HOLOGRAPHY WITH SPIN RESOLUTION

If the spin of an outgoing photoelectron can somehow be determined, either through its origin in a well-defined multiplet splitting [14] or through direct external measurement with respect to an external magnetization axis [16], then the spin-dependent aspects of photoelectron diffraction can be studied, for example, by comparing the patterns produced by exiting spin-up and spin-down electrons. These effects were first studied by Sinkovic et al. [14a], who made use of multiplet-split levels to provide the spin resolution. Experimental data from these studies [14a-c] provided evidence for a high-temperature loss of surface short-range antiferromagnetic order that had not been observed previously. Recent Monte Carlo calculations on such antiferromagnetic surfaces by Zhang et al. [41] further suggest that these measurements were in fact observing a surface Neél temperature several times that of the bulk. Beyond providing a new method for studying short-range magnetic order near surfaces, such spin-dependent photoelectron scattering and diffraction will also clearly be an important part of the analysis of MCD data such as that described in the last section.

In two recent studies the additional possibility of spin-polarized photoelectron holography has been considered [42]. Although there is as yet no experimental data on this subject, Kaduwela et al. [42a] have carried out model calculations on simple clusters. Some of these results are shown in Fig. 11 for a two-atom cluster in which one Mn^{2+} ion is the emitter and the other is a magnetically-ordered scatterer. In order to look for spin-dependent exchange effects in the scattering, Fourier-transform images U(x,y,z) were first calculated from Eq. 9 for outgoing spin-up and spin-down electrons; no scattered-wave correction was used in order to focus on the spin-dependent differences in the images. The kinetic energy was held constant at 120 eV for both cases. An exchange interaction with the five parallel-coupled 3d electrons was included in the scattering potential if the photoelectron spin was parallel to the net spin of the Mn^{2+} scatterer (↑,↑ or ↓,↓), and was omitted if the photoelectron spin was antiparallel to the scatterer spin (↑,↓ or ↓,↑). The two simplest measures of these exchange effects in holographic images are:

$$\Delta(x,y,z,\uparrow-\downarrow,\uparrow) = U(x,y,z,\uparrow,\uparrow) - U(x,y,z,\downarrow,\uparrow), \qquad (15)$$

which is simply a difference of two normal images, and

$$\Delta'(x,y,z,\uparrow-\downarrow,\uparrow) = \left|F_\sigma(x,y,z,\uparrow,\uparrow) - F_\sigma(x,y,z,\downarrow,\uparrow)\right|, \qquad (16)$$

in which F_σ is the (complex) Fourier transform integral within U and the absolute value is taken after calculating the difference. The second spin argument here is the orientation of the scatterer, here chosen to be up. Through its sign, Δ can be shown to be sensitive to the orientation of the scatterer, whereas the always-positive Δ' can be shown to measure more directly the strength of the spin-dependent exchange scattering.

In Fig. 11, the image functions Δ and Δ' are plotted for the two different orientations of the scatterer: spin-up in parts (a.2)-(a.4) and spin-down in parts (b.2)-(b.4). The effects seen here are 10-15% of the magnitude of the peaks in the direct U images, and thus should be measurable, especially from higher-quality experimental data obtained with a next-generation synchrotron radiation source. As expected from their definitions, Δ and Δ' exhibit different behavior on flipping the scatterer spin: Δ changes in sign, whereas Δ' does not. Thus, it has been suggested that the locations of near-neighbor magnetic scatterers could be determined via Δ', and actual spin flips (e.g., as temperature is changed) could be detected via Δ [42]. In parts (c.1)-(c.4) and (d.1)-(d.4), the effect of adding a non-magnetic O^{2-} scatterer midway between the two Mn^{2+} ions, with the scatterer spin being down, is considered. Although the normal image function U shows a strong additional peak due to the non-magnetic scatterer, this peak is strongly suppressed in Δ', verifying that the latter should be useful for imaging only the magnetic scatterers in a system.

REFERENCES

+ Work supported by the U.S. Department of Energy, Basic Energy Sciences, Materials Science Division, under Contract DOE-AC03-76SF00098, and the Office of Naval Research, under Contracts N00014-90-J-1457 and N00014-92-J-1140.

[1] (a) C.S. Fadley, Phys. Scripta T17, 39 (1987); (b) C.S. Fadley in Synchrotron Radiation Research: Advances in Surface Science, edited by R.Z. Bachrach (Plenum, New York, 1993); (c) C.S. Fadley, Surf. Sci. Repts., December, 1993.

[2] (a) S.A. Chambers, Adv. in Phys. 40, 357 (1990); S.A. Chambers, Surf. Sci. Repts. 16, 261 (1992); (b) W.F. Egelhoff, Jr. in Critical Reviews in Solid State and Materials Sciences, 16, 213 (1990).

[3] H.P. Bonzel, Prog. in Surf. Sci. 42, 219 (1993).

[4] (a) L.J. Terminello, X.S. Zhang, Z.Q. Huang, S. Kim, A.E. Schach von Wittenau, K.T. Leung, and D.A. Shirley, Phys. Rev. B38, 3879 (1988); (b)

L.-Q. Wang, Z. Hussain, Z.Q. Huang, A.E. Schach von Wittenau, D.A. Shirley, and D.W. Lindle, Phys. Rev. B44, 13771 (1991); (c) Y. Zheng and D.A. Shirley, to be published.

[5] A.M. Bradshaw and D.P. Woodruff, Applications of Synchrotron Radiation: High-Resolution Studies of Molecules and Molecular Adsorbates on Surfaces, edited by W. Eberhardt (Springer-Verlag, Berlin, 1993), in press.

[6] A. Szöke, in Short Wavelength Coherent Radiation: Generation and Applications, edited by D.T. Attwood and J. Bokor, AIP Conference Proceedings No. 147 (AIP, New York, 1986).

[7] (a) J.J. Barton, Phys. Rev. Lett. 61, 1356 (1988); (b) J.J. Barton, J. Electron Spectrosc. 51, 37 (1990); (c) J.J. Barton, Phys. Rev. Lett. 67, 3106 (1991).

[8] (a) C.H. Li and S.Y. Tong, Phys. Rev. Lett. 42, 901 (1979); (b) J.J. Barton and D.A. Shirley, Phys. Rev. B32, 1892 (1985); and Phys. Rev. B32, 1906 (1985); (c) A.P. Kaduwela, G.S. Herman, D.J. Friedman and C.S. Fadley, Phys. Scripta 41, 948 (1990); (d) A.P. Kaduwela, D.J. Friedman, and C.S. Fadley, J. Electron Spectrosc. 57, 223 (1991); (e) A.P. Kaduwela, M.A. Van Hove, and C.S. Fadley, unpublished results.

[9] D.J. Friedman and C.S. Fadley, J. Electron Spectrosc. 51, 689 (1990).

[10] (a) P.J. Orders and C.S. Fadley, Phys. Rev. B27, 781 (1983); (b) M. Sagurton, E.L. Bullock, and C.S. Fadley, Phys. Rev. 30, 7332 (1984).

[11] J. Osterwalder, T. Greber, S. Hüfner, and L. Schlapbach, Phys. Rev. B41, 12495 (1990); S. Hüfner, J. Osterwalder, T. Greber, and L. Schlapbach, Phys. Rev. B42, 7350 (1990); G.S. Herman and C.S. Fadley, Phys. Rev. B43, 6792 (1991); T. Greber, J. Osterwalder, S. Hüfner, and L. Schlapbach, Phys. Rev. B44, 8958 (1991).

[12] G. Waddill, J.G. Tobin, H. Li, and S.Y. Tong, Phys. Rev. Lett. 70, 4150 (1993) and paper by J.G. Tobin in these Proceedings.

[13] (a) D. Sebilleau, M.C. Desjonqueres, D. Chaveau, C. Guillot, J. Lecante, G. Treglia, and D. Spanjaard, Surf. Sci. Lett. 185, L527 (1987); (b) A. Nilsson, H. Tillborg, and N. Mårtensson, Phys. Rev. Lett. 67, 1015 (1991); (c) K.U. Weiss et al., Phys. Rev. Lett. 69, 3196 (1992); (d) J.D. Denlinger, E. Rotenberg, U. Hessinger, M. Leskovar, and M.A. Olmstead, Appl. Phys. Lett. 62, 2057 (1993), and E. Rotenberg, J.D. Denlinger, U. Hessinger, M. Leskovar, and M.A. Olmstead, J. Vac. Sci. Tech. B11, 1444 (1993).

[14] (a) B. Sinkovic, B.D. Hermsmeier, and C.S. Fadley, Phys. Rev. Lett. 55, 1227 (1985); (b) B.D. Hermsmeier, J. Osterwalder, D.J. Friedman, and C.S. Fadley, Phys. Rev. Lett. 62, 478 (1989); (c) B.D. Hermsmeier, J. Osterwalder, D.J. Friedman, B. Sinkovic, T.T. Tran, and C.S. Fadley,

Phys. Rev. B42, 11895 (1990); (d) B. Sinkovic, D.J. Friedman, and C.S. Fadley, J. Magn. Magn. Mater. 92, 301 (1991).

[15] G. Schönhense, Physica Scripta T31, 255 (1990).

[16] F.U. Hillebrecht, R. Jungblut, and E. Kisker, Phys. Rev. Lett. 65, 2450 (1990).

[17] S. Valeri and A. Di Bona, Rev. del Nuovo Cimento 16, 1 (1993), and S. Valeri, paper in these Proceedings.

[18] G.R. Harp, D.K. Saldin, and B.P. Tonner, Phys. Rev. Lett. 65, 1012 (1990); C.M. Wei, I.H. Hong, P.R. Jeng, S.C. Shyu, and Y.C. Chou, private communication, and C.M. Wei, Y.C. Chou, I.H. Hong, P.R. Jeng, and S.C. Shyu, paper in these Proceedings.

[19] D.K. Saldin and P.L. de Andres, Phys. Rev. Lett. 65, 1012 (1990); K. Heinz, U. Starke, and F. Bothe, Surf. Sci. Lett. 243, 670 (1991); and K. Heinz, paper in these Proceedings.

[20] S. Thevuthasan, F. Zhang, R.X. Ynzunza, E.D. Tober, and C.S. Fadley, unpublished results.

[21] T. Hertel, T. Greber, and J. Osterwalder, unpublished results; S.D. Ruebush, R. Couch, H. Xiao, Z. Wang, S. Thevuthasan, and C.S. Fadley, unpublished results.

[22] O.M. Kuettel and J. Osterwalder, unpublished results.

[23] U. Breuer, O. Knauff, and H.P. Bonzel, J. Vac. Sci. Tech. A8, 2489 (1990); U. Breuer, H.P. Bonzel, K.C. Prince, and R. Lipowsky, Surf. Sci. 223, 258 (1989); T.T. Tran, S. Thevuthasan, Y.J. Kim, G.S. Herman, D.J. Friedman, and C.S. Fadley, Phys. Rev. B45, 12106 (1992); T.T. Tran, S. Thevuthasan, Y.J. Kim, D.J. Friedman, A.P. Kaduwela, G.S. Herman, and C.S. Fadley, Surf. Sci. 281, 270 (1993).

[24] (a) V. Fritzsche and D.P. Woodruff, Phys. Rev. B46, 16128 (1992); (b) P. Hofmann and K.M. Schindler, Phys. Rev. B 47, 13942 (1993).

[25] B.P. Tonner, Z.-L. Han, G.R. Harp, and D.K. Saldin, Phys. Rev. B43, 14423 (1991).

[26] (a) G.R. Harp, D.K. Saldin, and B.P. Tonner, Phys. Rev. Lett. 65, 1012 (1990); (b) G.R. Harp, D.K. Saldin, and B.P. Tonner, Phys. Rev. B42, 9199 (1990).

[27] (a) G.S. Herman, S. Thevuthasan, T.T. Tran, Y.J. Kim, and C.S. Fadley, Phys. Rev. Lett. 68, 650 (1992); (b) S. Thevuthasan, G.S. Herman, A.P. Kaduwela, T.T. Tran, Y.J. Kim, R.S. Saiki, and C.S. Fadley, J. Vac. Sci. Technol. A10, 2261 (1992); (c) S. Thevuthasan, R.X. Ynzunza, E.D. Tober, C.S. Fadley, A.P. Kaduwela, and M.A. van Hove, Phy. Rev. Lett. 70, 595 (1993).

[28] Y. Zhou, X. Chen, J.C. Campuzano, G. Jennings, H. Ding, and D.K. Saldin, Mat. Res. Soc. Symp. Proc. 307, 279 (1993).

[29] (a) L.J. Terminello, J.J. Barton, and D.A. Lapiano-Smith, J. Vac. Sci. Technol. B10, 2088 (1992) and Phys. Rev. Lett. 70, 599 (1993). (b) B.L. Petersen, L.J. Terminello, and D.A. Shirley, Mat. Res. Soc. Symp. Proc. 307, 285 (1993), and private communication.

[30] H. Wu, G.J. Lapeyre, H. Huang, and S.Y. Tong, Phys. Rev. Lett. 71, 251 (1993).

[31] J. Osterwalder, to be published.

[32] (a) S. Thevuthasan, G.S. Herman, A.P. Kaduwela, R.S. Saiki, Y.J. Kim, W. Niemczura, M. Burger and C.S. Fadley, Phys. Rev. Lett. 67, 469 (1991) (b) S. Thevuthasan, P.M. Len, and C.S. Fadley, to be published.

[33] G.R. Harp, D.K. Saldin, X. Chen, Z.L. Han, and B.P. Tonner, J. Electron Spectrosc. 258, 313 (1991).

[34] D.K. Saldin, G.R. Harp, and B.P. Tonner, Phys. Rev. B45, 9629 (1992); (b) S.Y. Tong, C.M. Wei, T.C. Zhao, H. Huang, and H. Li, Phys. Rev. Lett. 66, 60 (1991).

[35] D.K. Saldin, G.R. Harp, B.L. Chen and B.P. Tonner, Phys. Rev. B44, 2480 (1992).

[36] R.S. Saiki, A.P. Kaduwela, J. Osterwalder, D.J. Friedman, C.S. Fadley, and C.R. Brundle, Surf. Sci. 279, 305 (1992).

[37] S.Y. Tong, H. Li, and H. Huang, Phys. Rev. Lett. 67, 3102 (1992); S.Y. Tong, H. Huang, and C.M. Wei, Phys. Rev. B46, 2452 (1992).

[38] P.M. Len, S. Thevuthasan, and C.S. Fadley, unpublished results.

[39] (a) J. Bansmann, Ch. Ostertag, G. Schönhense, F. Fegel, C. Westphal, M. Getzlaff, F. Schafers, and H. Petersen, Phys. Rev. B46, 13496 (1992) and V. McKoy, private communication; (b) C. Westphal, A.P. Kaduwela, M.A. Van Hove, and C.S. Fadley, to be published.

[40] (a) G. Baumgarten, C.M. Schneider, H. Petersen, F. Schafers, and J. Kirschner, Phys. Rev. Lett. 65, 492 (1990); (b) G.D. Waddill, J. Tobin, and D.R. Pappas, Phys. Rev. B46, 552 (1992).

[41] F. Zhang, S. Thevuthasan, R. Scalettar, R. Singh, and C.S. Fadley, to be published.

[42] (a) A.P. Kaduwela, Z. Wang, M.A. Van Hove, and C.S. Fadley, to be published; (b) E.M.E. Timmermans, G.T. Trammell, and J.P. Hannon, private communication.

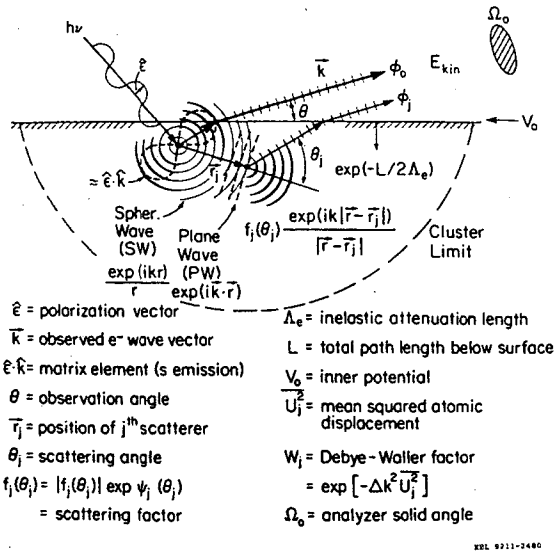

Fig. 1- The basic process involved in photoelectron diffraction, with important physical variables indicated. Only single scattering is indicated for simplicity. In a holographic interpretation of such measurements, the direct or unscattered wave ϕ_o is identified with the reference wave, and the scattered waves ϕ_j are identified with object(subject) waves.

Ni(001):Ni 2p at 636 eV

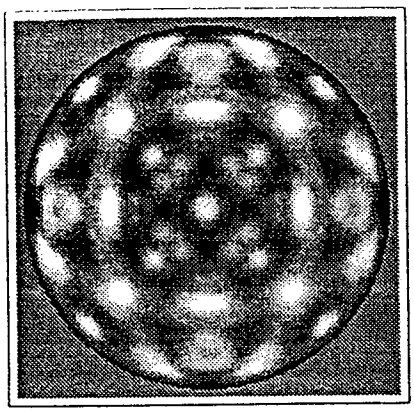

Ru(0001):Ru 3d at 1206 eV

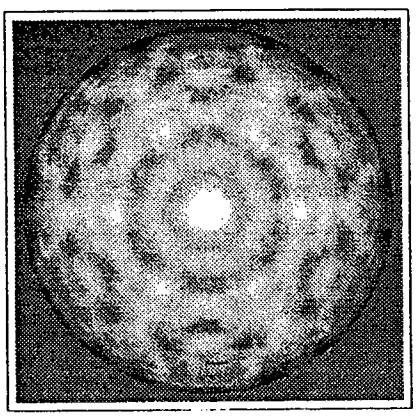

Graphite (0001): C 1s at 946 eV

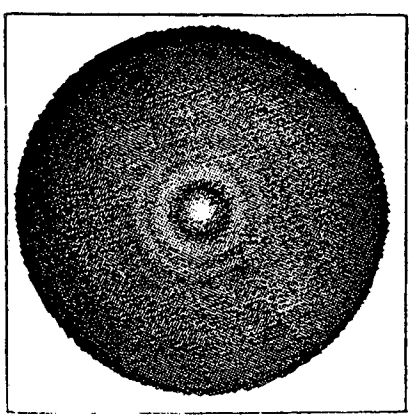

Fig. 2- Full 2π intensity distributions for higher-energy emission from several surfaces: fcc Ni(001) [ref. 20], hcp Ru(0001) [ref. 21], and highly oriented pyrolytic graphite in textured growth with preferred (0001) orientation [ref. 22].

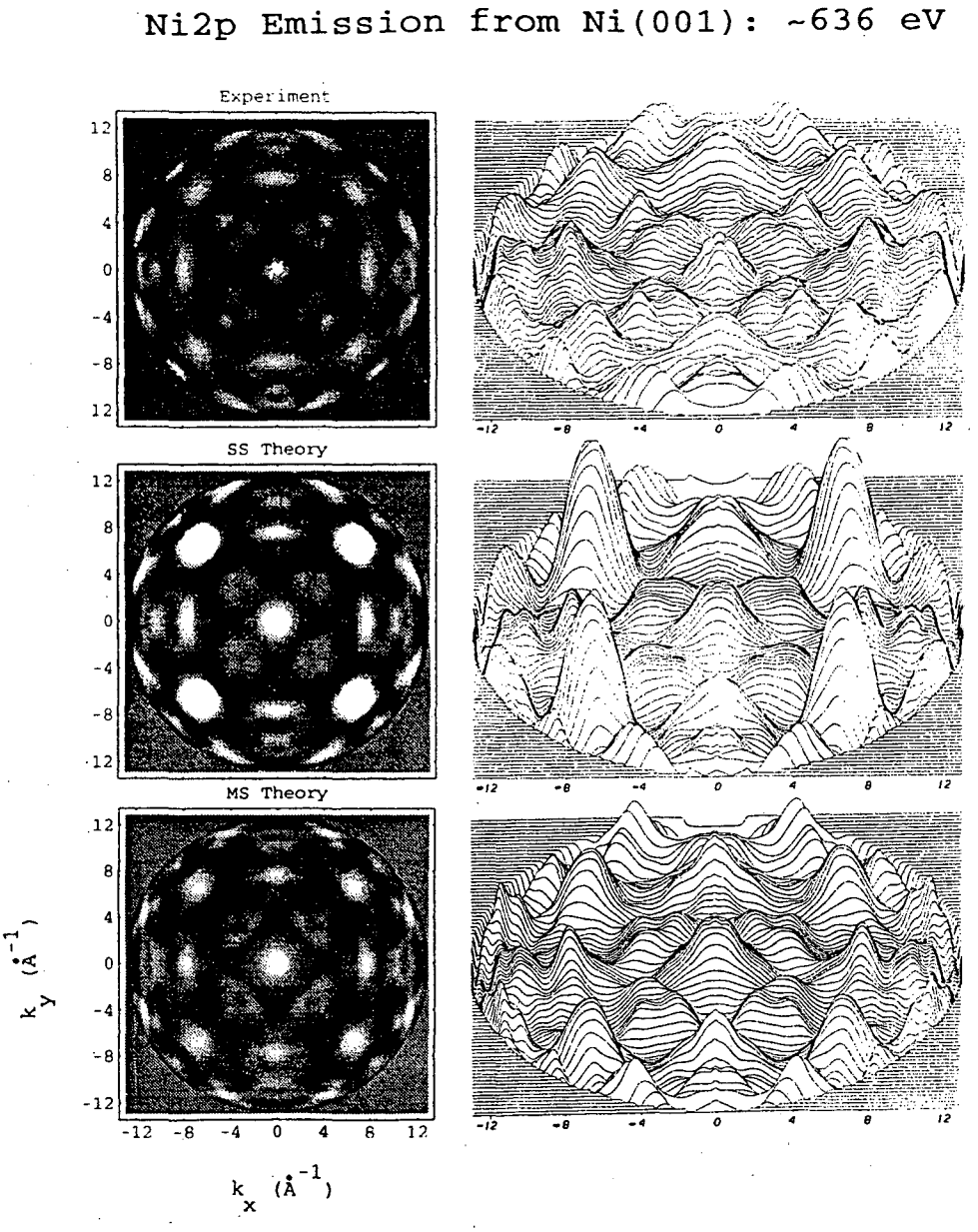

Fig. 3- The Ni $2p_{3/2}$ intensity above a Ni(001) surface as excited by Al Kα radiation: experimental data are compared with single scattering theory and multiple scattering theory. [From Thevuthasan et al., ref. 20]

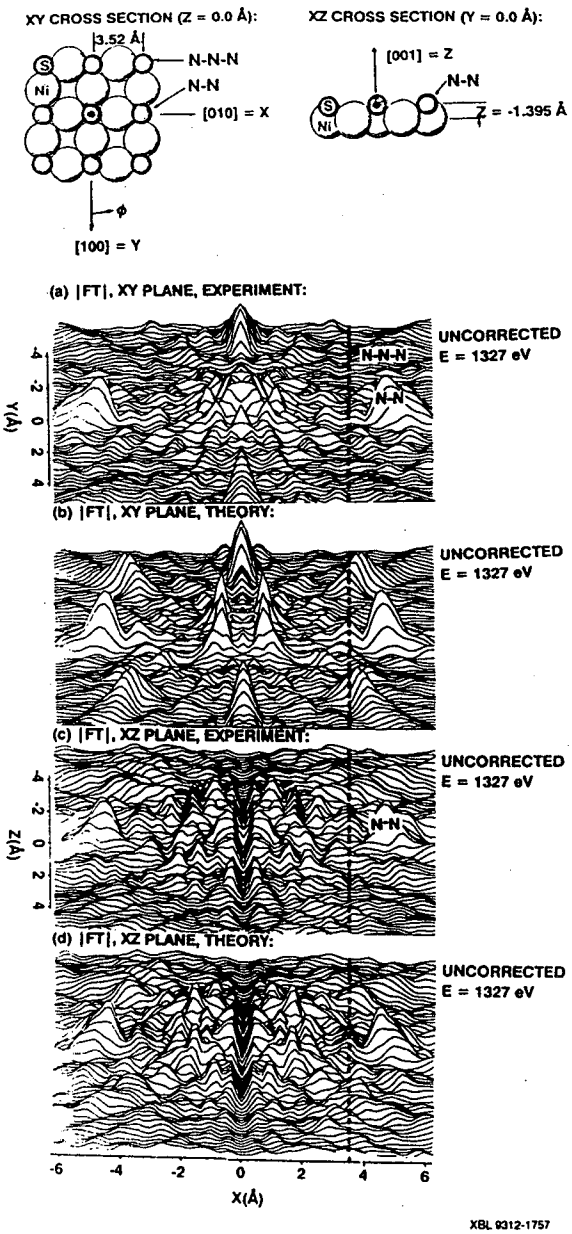

Fig. 4- The geometry of c(2x2)S/Ni(001) is shown together with Fourier transform holographic images from Eq. 10, as based upon S 2p emission at 1327 eV. The hologram analyzed has cylindrical symmetry about the z axis, and extends from 10° to 50° above the surface. Images are shown in both the xy (=sulfur) and xz planes. No scattered-wave correction has been made, and results are shown for both experiment ((a) and (c)) and single-scattering theory ((b) and (d)). The positions of nearest-neighbor (N-N) and next-nearest-neighbor (N-N-N) S atoms are indicated. The vertical dashed line indicates the known positions of these atoms. [From Thevuthasan et al. ref. 27c]

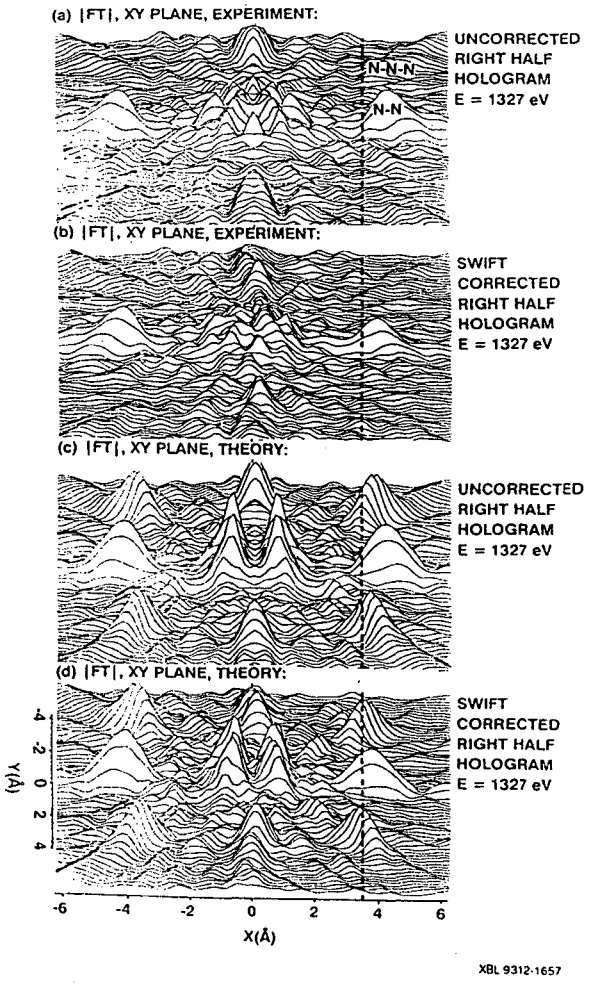

Fig. 5- Fourier transform images in the S plane of c(2x2)S/Ni(001) based upon S 2p emission at 1327 eV. Only the right half of the hologram used in Fig. 4 has been analyzed to minimize real/twin overlap, and the SWIFT scattered-wave correction of Eq. 11 has been used in (b) and (d). Experimental results have been used to derive the images in (a) and (b), and single-scattering theory in (c) and (d). [From Thevuthasan et al., ref. 27c]

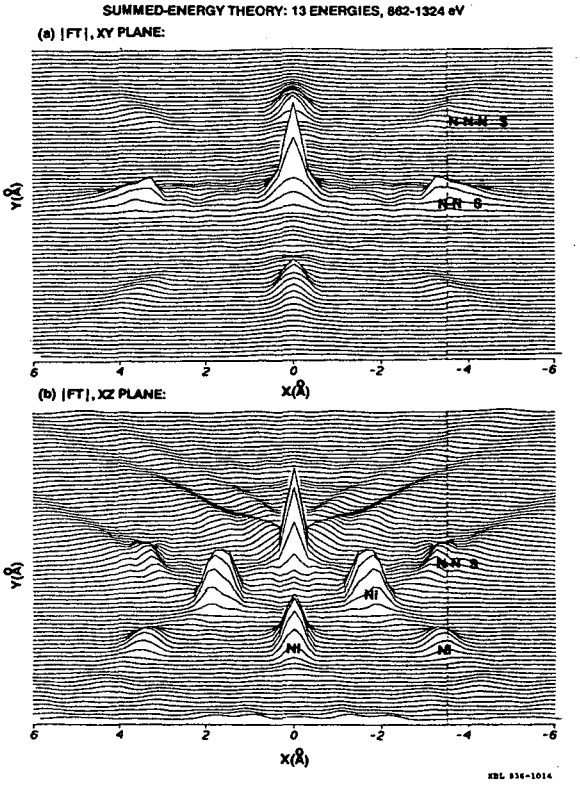

Fig. 6- Theoretical Fourier transform images in the xy (=sulfur) and xz planes based on S 2p emission from c(2x2)S/Ni(001). The hologram spanned the more ideal scattering region from 30° above the surface to the surface normal. A phased sum of transforms according to Eq. 12b has been made over 13 energies between 862 and 1324 eV. [From Thevuthasan et al., ref. 32b]

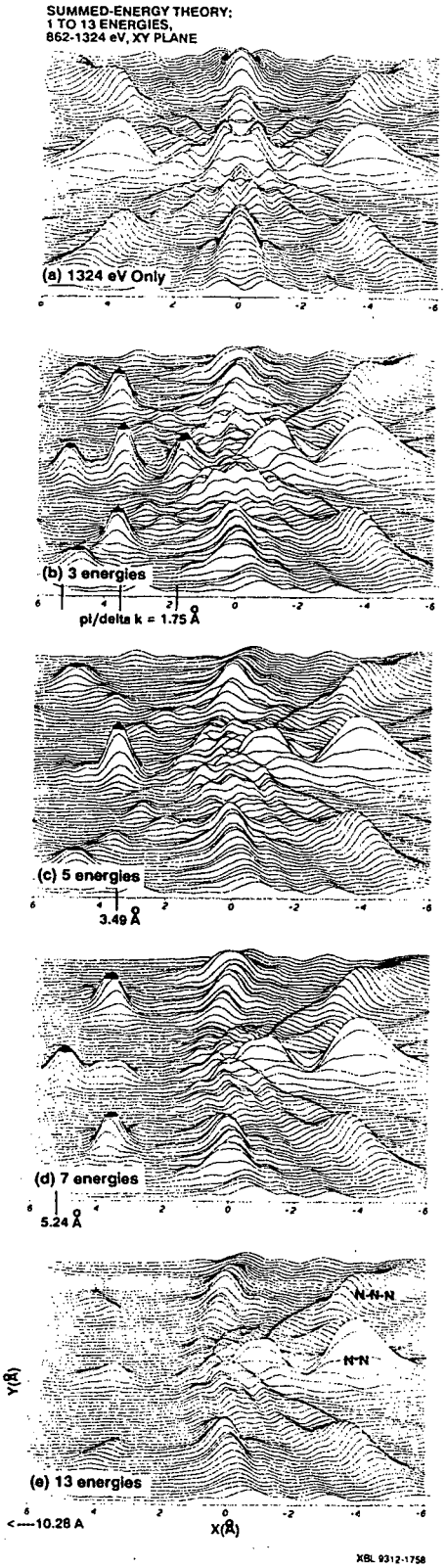

Fig. 7- Theoretical Fourier transform images for c(2x2)S/Ni(001) in the S plane obtained using only the right half of a hologram extending from 10° to 50° above the surface (as in Figs. 4 and 5). Data are shown for different numbers of energies in a phased sum according to Eq. 12b, but with no scattered-wave correction: (a) 1 energy, (b) = 3 energies, (c) = 5, (d) = 7, and (e) = 13. The multiples of $\pi/\delta k$ at which artifacts can remain on spherical surfaces surrounding the origin are also indicated; the shaded peaks all occur at such positions. [From Thevuthasan et al., ref. 32b]

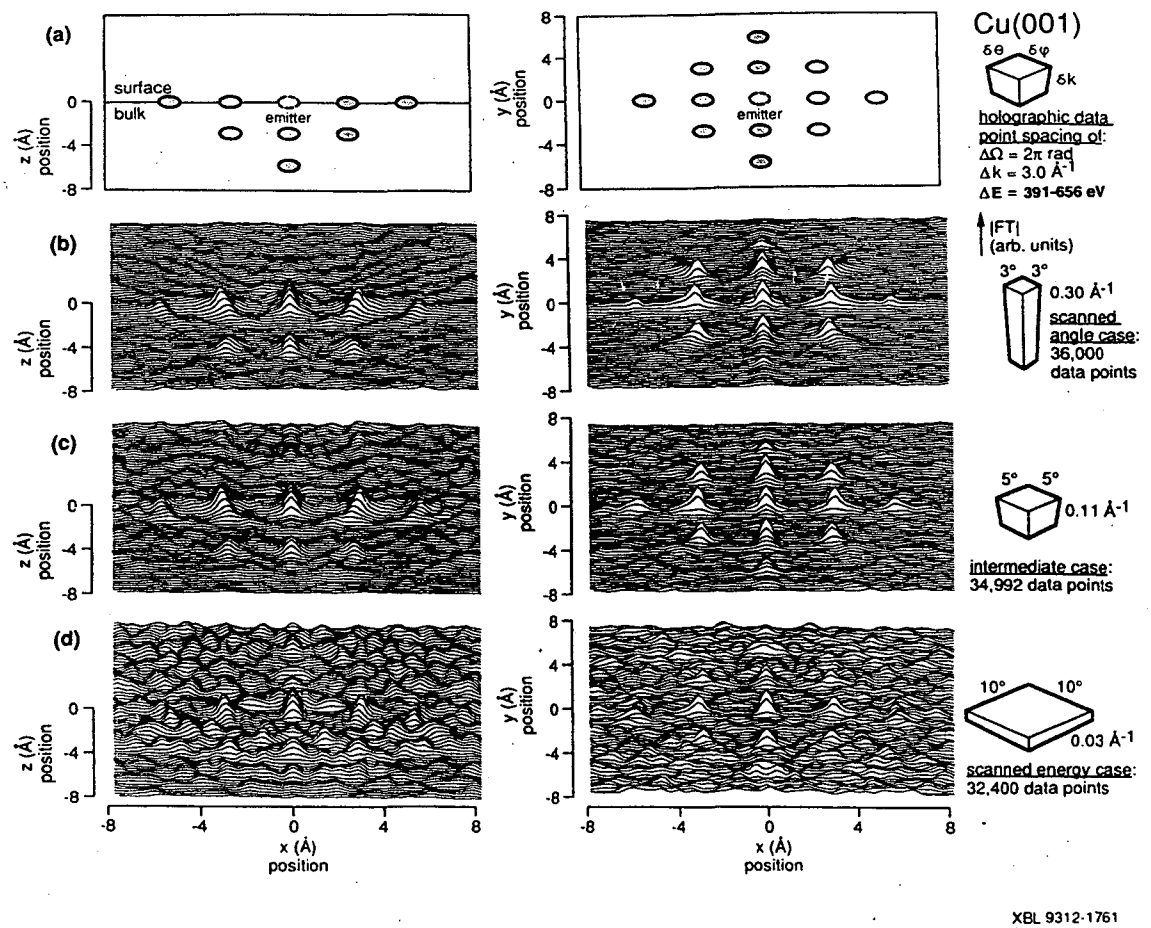

Fig. 8- Multi-energy theoretical holographic images derived from Eq. 12 (or equivalently Eq. 13) for a single emitter in the center of a pyramidal Cu cluster simulating the (001) surface. Full 2π holograms have been calculated and the total ranges in $\underline{k}$ and E considered have been kept constant at 3.0 $Å^{-1}$ and 391-656 eV, respectively. The total number of data points also has been held nearly constant, but the sampling of $\underline{k}$ space is varied from (b) = dense in direction ("scanned-angle") to (d) = dense in energy ("scanned-energy"). The sampling volume element is defined by $\delta\theta$ and $\delta\phi$ in degrees, and δk in $Å^{-1}$. The number of energies involved is 11 in (b), 28 in (c), and 101 in (d). [From Len et al., 38]

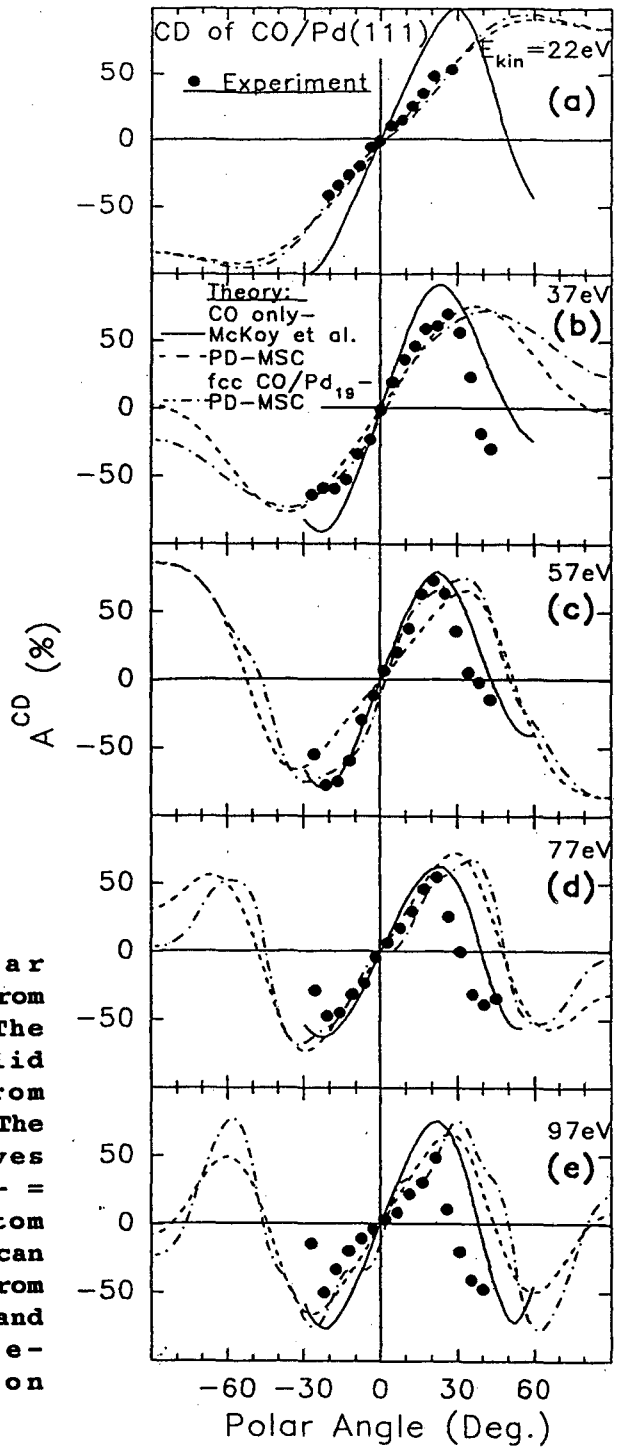

Fig. 9- Normal circular dichroism in C 1s emission from CO adsorbed on Pd(111). The experimental data and solid theoretical curve are from Bansmann et al. [ref. 39a]. The other two theoretical curves (------ = CO only and - --- - = CO in fcc sites on a 19-atom Pd(111) cluster, with the θ scan in the [10,-1] azimuth) are from Westphal et al. [ref. 39b] and are based upon multiple-scattering photoelectron diffraction calculations.

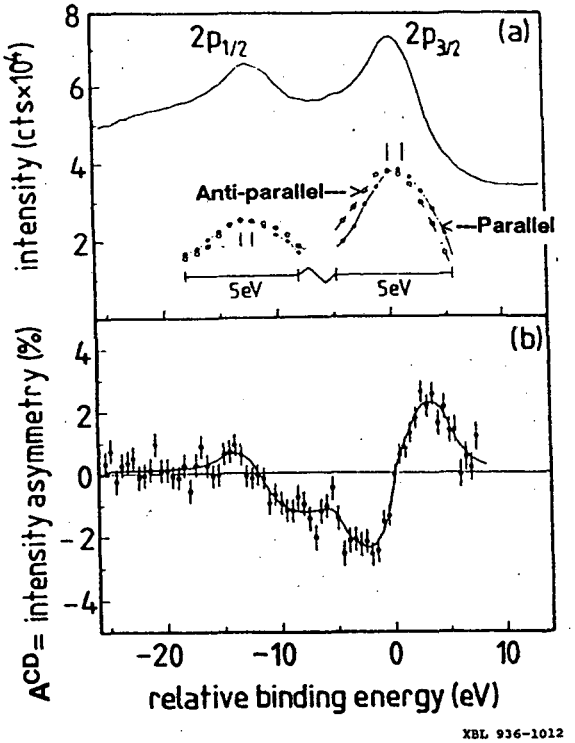

Fig. 10- Magnetic circular dichroism in Fe 2p emission from Fe(110). In (a), the average full spectrum is shown together with data for photon incidence parallel-to and anti-parallel-to the specimen magnetization. In (b), the asymmetry as calculated from Eq. 14 is plotted. [From Baumgarten et al., ref. 40a]

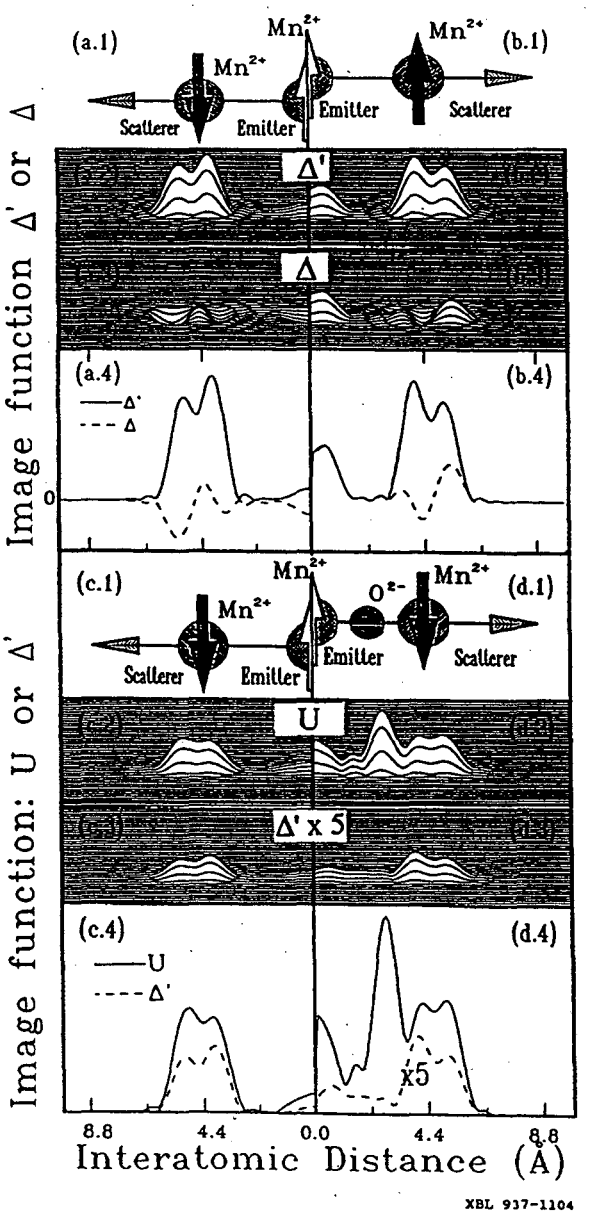

Fig. 11- Theoretical spin-polarized holographic images based upon the (spin-up) - (spin-down) difference functions Δ (Eq. 15) and Δ' (Eq. 16) for a cluster of two Mn^{2+} ions consisting of an emitter and scatterer that are 4.4 Å apart. The outgoing electron energy is 120 eV for both spin-up and spin-down. (a.1)-(a.4) are for the scatterer spin down. (b.1)-(b.4) are for the scatterer spin down. In (c.1)-(c.4) and (d.1)-(d.4), the effect of including a non-magnetic O^{2-} scatterer on both the usual image function U and on Δ' are illustrated. [From Kaduwela et al., ref. 42a]

LAWRENCE BERKELEY LABORATORY
UNIVERSITY OF CALIFORNIA
TECHNICAL INFORMATION DEPARTMENT
BERKELEY, CALIFORNIA 94720